2

The linear instability problem

This chapter summarizes the well-known (e.g., Baines and Gill, 1969; Walin, 1964; Nield, 1967) results of linear stability analysis for a basic state with uniform temperature and salinity gradients. There is a consensus that the choice of boundary conditions has little effect on linear stability characteristics as long as the size of a double-diffusive layer greatly exceeds the nominal double-diffusive scale d in (1.8). Therefore, our review is restricted to the simplest configuration – the unbounded gradient layer model.

2.1 Conditions for instability

Consider a motionless, laterally homogeneous layer, which is vertically stratified in either the fingering ($\bar{T}_z > 0$, $\bar{S}_z > 0$) or diffusive ($\bar{T}_z < 0$, $\bar{S}_z < 0$) sense. We assume that the perturbation to the basic state is weak and therefore the non-dimensional governing equations (1.12) and (1.13) are linearized by neglecting the advective terms $\vec{v}' \cdot \nabla T'$, $\vec{v}' \cdot \nabla S'$ and $\vec{v}' \cdot \nabla \vec{v}'$ in the temperature, salinity and momentum equations (perturbations are denoted by primes). Stability of the resulting linear system is examined using the normal modes:

$$(T', S', \vec{v}', \ p') = \text{Re}\big[(\hat{T}, \hat{S}, \hat{\vec{v}}, \hat{p}) \exp(\lambda t + ikx + ily + imz)\big], \qquad (2.1)$$

where λ is the growth rate and $\vec{k} = (k, l, m)$ is the wavenumber; the spatially uniform amplitudes of Fourier components are denoted by hats. When the normal modes (2.1) are substituted in the linearized system and the amplitudes $(\hat{T}, \hat{S}, \hat{\vec{v}}, \hat{p})$ are sequentially eliminated, we arrive at the eigenvalue equations:

salt fingers

$$\lambda^3 + [1 + \tau + Pr]\kappa^2\lambda^2 + \big[(\tau + Pr + \tau Pr)\kappa^4 + Prk_H^2\kappa^{-2}\big(1 - R_\rho^{-1}\big)\big]\lambda$$
$$+ \tau Pr\kappa^6 - Prk_H^2\big(R_\rho^{-1} - \tau\big) = 0,$$

diffusive convection

$$\lambda^3 + [1 + \tau + Pr]\kappa^2\lambda^2 + \left[(\tau + Pr + \tau Pr)\kappa^4 - Prk_H^2\kappa^{-2}\left(1 - R_\rho^{-1}\right)\right]\lambda$$
$$+ \tau Pr\kappa^6 + Prk_H^2\left(R_\rho^{-1} - \tau\right) = 0, \quad (2.2)$$

where $\kappa = |\vec{k}|$ and $k_H = \sqrt{k^2 + l^2}$. For instability to occur, $\text{Re}(\lambda) > 0$ for some wavenumbers ($\vec{k}$).

Our stability analysis becomes analytically tractable when we take advantage of a simple algebraic property of (2.2) – the growth rate equations are invariant with respect to the transformation

$$\lambda \to a\lambda, \quad \kappa^2 \to a\kappa^2, \quad k_H^2 \to a^3 k_H^2, \quad (2.3)$$

where a is an arbitrary positive constant. Choosing $a = \frac{\kappa}{k_H} > 1$ in (2.3), we can transform any wavenumber $\vec{k}$ to the one with $\kappa = k_H$ or, equivalently, with $m = 0$. The new wavenumber represents a vertically oriented (z-independent) harmonic, also known as the elevator mode. The original growth rate can be recovered by dividing λ of the transformed mode by $a > 1$. A corollary of the invariance relation (2.3) is that the stability of our system needs only to be examined, without loss of generality, for the elevator modes – a small subset of all Fourier harmonics in (2.1). The growth rates of tilted modes with finite m are smaller than those of their vertical counterparts but have the same sign.

After restricting analysis to the rapidly growing elevator modes ($m = 0$), the instability conditions are obtained by requiring $\text{Re}(\lambda) = 0$ at the marginal instability point, resulting in

$$\begin{aligned} 1 &< R_\rho < \frac{1}{\tau} && \text{for salt fingering,} \\ 1 &< R_\rho^* = R_\rho^{-1} < \frac{Pr + 1}{Pr + \tau} && \text{for diffusive convection.} \end{aligned} \quad (2.4)$$

As previously, we consider only gravitationally stable (bottom-heavy) configurations, which accounts for the lower limit of unity for the density ratios in (2.4).

In the oceanographic (heat–salt) case, the diffusivity ratio is $\tau \approx 0.01$, and therefore (2.4) suggests a wide range of finger-favorable density ratios ($1 < R_\rho < 100$). These conditions are met, for instance, in more than 90% of the Atlantic thermocline. On the other hand, the range of diffusive convection ($1 < R_\rho^* < 1.14$) is extremely narrow. Both predictions, however, should be interpreted cautiously. As we shall see later on (Chapters 3–5), finite amplitude effects, not considered in linear theory, have a profound effect on the distribution and intensity of double-diffusive convection. For salt fingering, nonlinearity constrains the amplitude of perturbations and makes finger-driven mixing rather ineffective for $R_\rho > 2$. The diffusive range predicted by (2.4) can also be misleading. In the ocean, diffusive

convection appears more frequently in the form of diffusive layering and the conditions for its maintenance ($R_\rho^* < 10$) are less restrictive than for linear oscillatory instability.

It is instructive to express the instability conditions (2.4) in terms of the Turner angle (Section 1.6). For salt fingers (heat–salt case) the linear instability range is $45.57° < Tu < 90°$, which constitutes 99% of the $\bar{T}_z > 0$, $\bar{S}_z > 0$ sector (Fig. 1.7). This implies that stratification patterns in which temperature and salinity increase upward are most likely to support fingering instability. The situation is markedly different for diffusive convection. The linearly unstable region is $-90° < Tu < -86.26°$, which means that only a small fraction (8.3%) of the diffusive sector ($\bar{T}_z < 0$, $\bar{S}_z < 0$) is susceptible to small-amplitude oscillatory instability.

2.2 Growth rates and spatial scales

Having established conditions for the onset of double-diffusive instabilities, we now proceed to analyze growth rates and preferred spatial patterns along the lines of Schmitt (1979a). Our focus is on fingering (rather than diffusive) instability, which is motivated by the utility and relevance of linear stability analysis. Stability theory successfully explains several key characteristics of salt fingers inferred from field measurements and laboratory experiments, while the connection between primary diffusive instabilities and observed structures is less clear. Following the conventional approach in linear stability models, we concentrate on the unstable mode with the largest growth rate. This methodology is based on a sensible assumption: If a weak initial perturbation contains a full spectrum of normal modes, then the fastest growing mode is more likely to reach the level of nonlinear equilibration first and thereby determine the pattern of fully developed instability.

Since the largest growth rates are always attained by the vertically homogeneous elevator modes, we assume $m = 0$, which reduces the fingering growth rate equation in (2.2) to

$$\lambda^3 + [1 + \tau + Pr]\,k_H^2\lambda^2 + \left[(\tau + Pr + \tau Pr)\kappa^4 + Pr\left(1 - R_\rho^{-1}\right)\right]\lambda$$
$$+ \tau Prk_H^6 - Prk_H^2\left(R_\rho^{-1} - \tau\right) = 0. \tag{2.5}$$

The most unstable mode is determined by maximizing $\mathrm{Re}(\lambda)$ over the three roots of the cubic in (2.5) for given (R_ρ, τ, Pr). The typical dependence of λ on k_H is shown in Figure 2.1. The growth rate is real, which signifies the direct mode of instability, characterized by monotonic growth of perturbations. The basic state is unstable for a finite range of not-too-large wavenumbers and the growth rate pattern is characterized by a well-defined maximum λ_{max} at the wavenumber k_{max}.
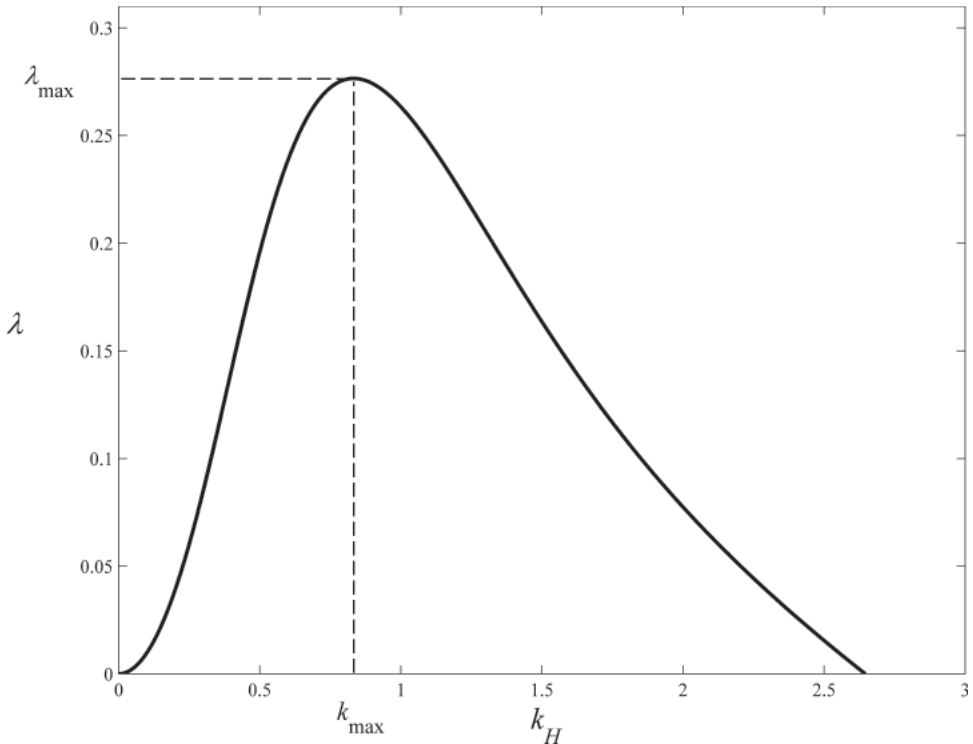
Figure 2.1 The growth rate (λ) of the elevator modes in the fingering regime as a function of the horizontal wavenumber (k_H) for $(R_\rho, Pr, \tau) = (2, 7, 0.01)$. Note the well-defined maximum ($\lambda_{\max}$) at $k_H = k_{\max}$.

This maximal growth rate is plotted as a function of density ratio in Figure 2.2. As expected, $\lambda_{\max}$ monotonically decreases with increasing R_ρ – fingering is most intense when the destabilizing salinity gradient is large and is adversely affected by the stabilizing gradient of temperature. The growth rates in Figure 2.2 are presented in standard non-dimensional units (1.11) and also in the dimensional form for $\bar{T}_z = 0.01$ °C m^{-1}, which is the typical stratification in the main mid-latitude thermocline. Salt fingers grow on the time scale of 10–20 minutes and therefore they are able to rapidly adjust to changing background conditions.

Figure 2.3 presents the wavenumber $k_{\max}$, along with the corresponding dimensional wavelength $L_{\dim}$, as a function of R_ρ. The fastest growing finger wavelength is on the order of a few centimeters and is only weakly dependent on the density ratio. A number of studies (Magnell, 1976; Gargett and Schmitt, 1982) find close agreement between the finger scales predicted by linear analysis and those inferred from field measurements. Note that the non-dimensional values of $\lambda_{\max}$ and $k_{\max}$ in Figures 2.2 and 2.3 are of order unity, which is consistent with the spatial and
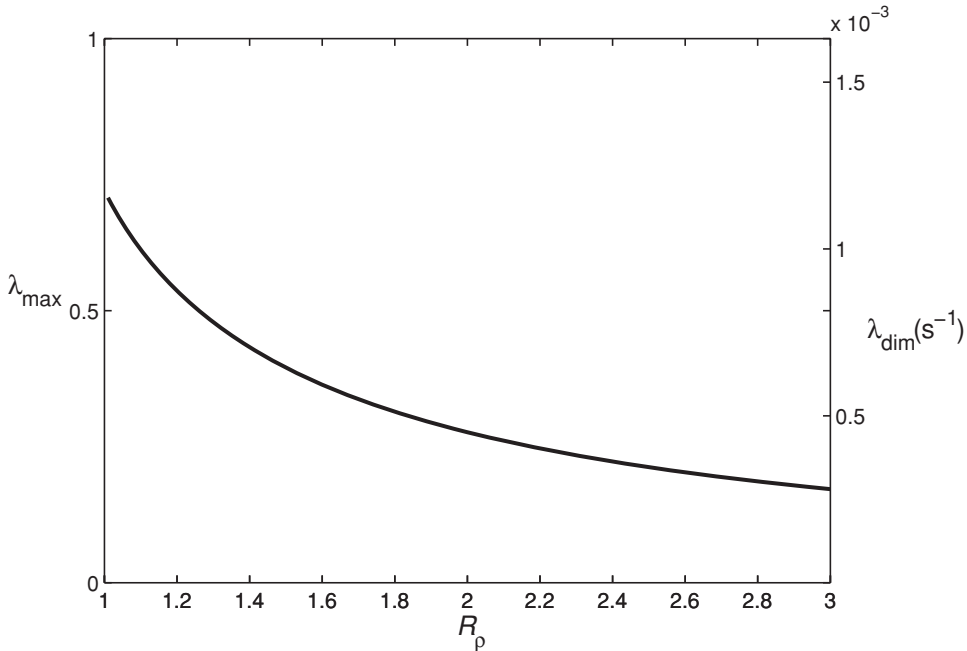
Figure 2.2 The maximal growth rate of salt fingers as a function of the density ratio. Non-dimensional values are indicated on the left axis. The right axis shows dimensional growth rates evaluated for the background temperature gradient of $\bar{T}_z = 0.01\,^\circ\mathrm{C}\,\mathrm{m}^{-1}$.

temporal scaling established in (1.7). Figure 2.4 shows the growth rate as a function of k_H and R_ρ, indicating the sensitivity of primary instability to both the finger scale and the background stratification. Overly thin fingers are damped by viscosity and ultimately by salt diffusion. Wide fingers do not lose enough heat laterally to fully engage double-diffusive mechanics and therefore they cannot grow as fast as intermediate width fingers.

It should be emphasized that, for a given background state, λ is uniquely determined by k_H. Hence, any combination of horizontal wavenumbers (k, l) satisfying

$$k^2 + l^2 = k_{max}^2 \tag{2.6}$$

results in the identical maximal growth rate λ_{max}, as does any linear superposition of normal modes satisfying (2.6). Thus, a variety of horizontal patterns have the same selective advantages and a-priori equal chances of controlling the fully developed state. This degeneracy of linear double-diffusive systems leads to very interesting and challenging theoretical problems regarding the horizontal planform selection of salt fingers (Proctor and Holyer, 1986; Schmitt, 1994a; Radko and Stern, 2000).
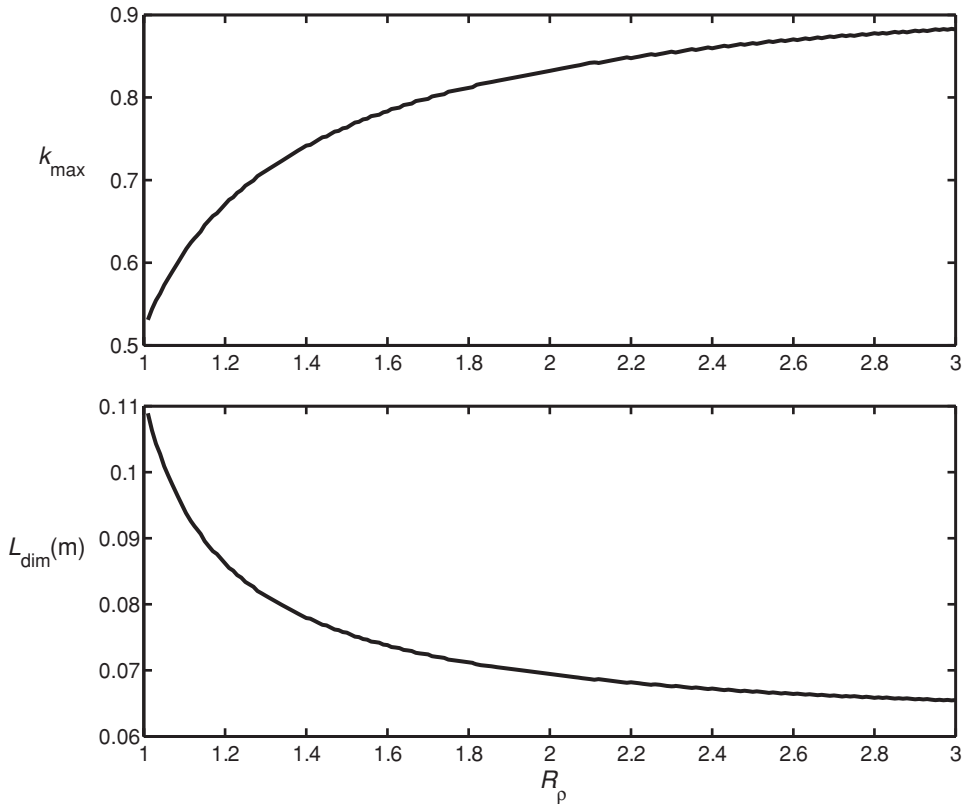
Figure 2.3 The top panel presents the wavenumber of the fastest growing elevator mode as a function of the density ratio. The bottom panel shows the corresponding dimensional wavelength evaluated for $\bar{T}_z = 0.01 \, °\mathrm{C}\,\mathrm{m}^{-1}$.

The preferred planform can only be predicted by invoking fundamentally nonlinear considerations (Chapter 5).

The stability properties of salt fingers should be contrasted with those of diffusive convection. An example of a diffusive solution is presented in Figure 2.5, where we plot real and imaginary components of $\lambda_{\max}$ as functions of R_ρ^*. Unlike in the salt-finger case, where λ is real, $\mathrm{Im}(\lambda)$ now significantly exceeds $\mathrm{Re}(\lambda)$. Since $\mathrm{Im}(\lambda)$ is associated with the oscillatory pattern of motion, diffusive modes are best described as periodic waves of gradually increasing amplitude.

2.3 The flux ratio

One of the most widely used and best understood characteristics of double-diffusive convection is represented by the flux ratio, which measures the fraction of the
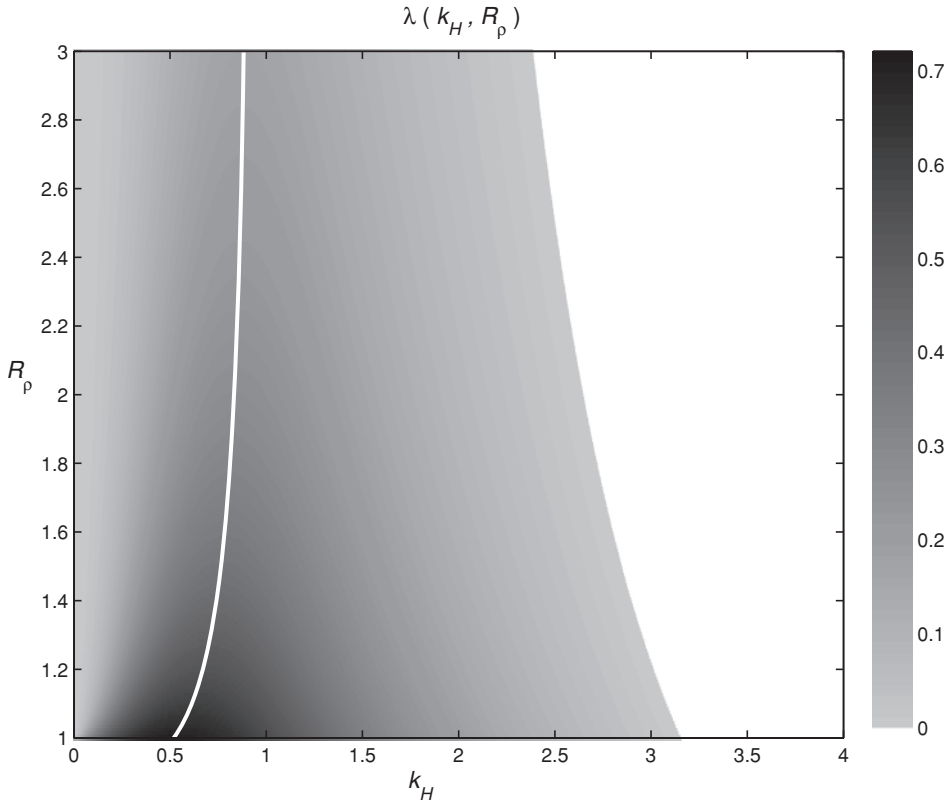
$$\lambda\,(\,k_H\,,\,R_\rho\,)$$

Figure 2.4 The growth rate of the elevator modes as a function of k_H and R_ρ. Only amplifying modes are shown. The white curve indicates the wavenumber of the fastest growing mode (k_{max}).

destabilizing component's potential energy loss gained by the stabilizing substance. In the fingering regime ($\bar{T}_z > 0$, $\bar{S}_z > 0$) the flux ratio takes the form

$$\gamma = \frac{\alpha F_{T\,dim}}{\beta F_{S\,dim}}, \tag{2.7}$$

where ($F_{T\,dim}$, $F_{S\,dim}$) are the dimensional vertical fluxes of temperature and salinity. The corresponding expression for the diffusive case ($\bar{T}_z < 0$, $\bar{S}_z < 0$) is given by

$$\gamma^* = \frac{\beta F_{S\,dim}}{\alpha F_{T\,dim}}. \tag{2.8}$$

The *T–S* fluxes in (2.7) and (2.8) include the contribution from transient eddies as well as molecular transport:

$$F_{T\,dim} = \overline{w'_{dim} T'_{dim}} + k_T \bar{T}_z,$$
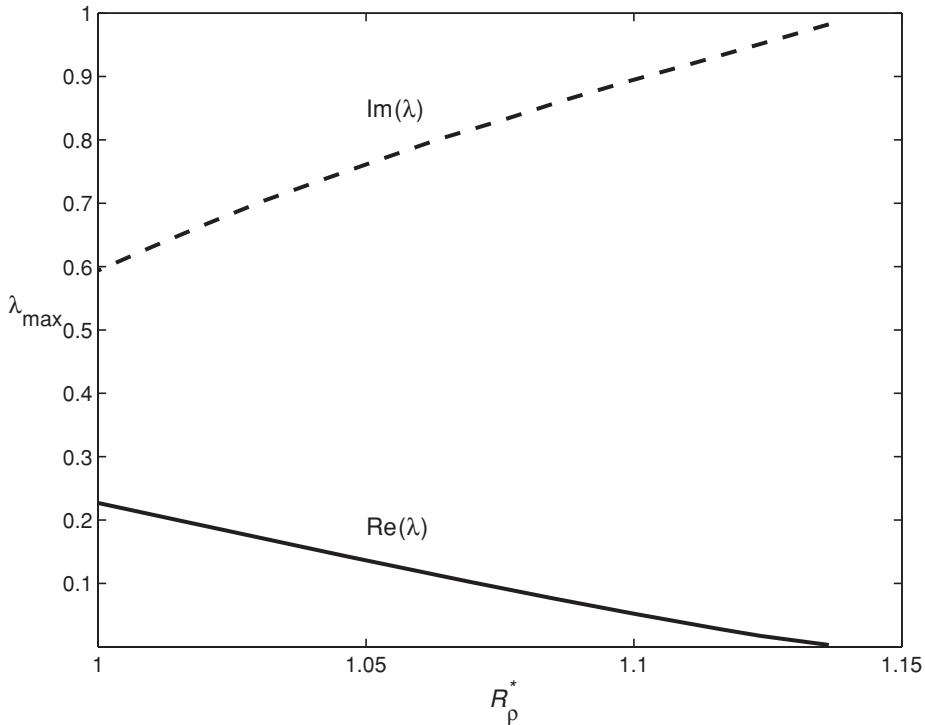$$F_{S\,dim} = \overline{w'_{dim} S'_{dim}} + k_S \bar{S}_z, \tag{2.9}$$

Figure 2.5 Diffusive convection. Real and imaginary components of the growth rate of the fastest growing mode are plotted as a function of the density ratio.

where the overbars denote spatial averages. However, very often, particularly in oceanographic applications, fluxes are dominated by their eddy-induced components $(\overline{w'_{\text{dim}} T'_{\text{dim}}}, \overline{w'_{\text{dim}} S'_{\text{dim}}})$. Neglecting molecular transport in (2.9) and applying the standard double-diffusive non-dimensionalization (1.11), we reduce the expression for the flux ratio to

$$\gamma \approx \frac{\overline{w'T'}}{\overline{w'S'}}. \tag{2.10}$$

From a theoretical standpoint, an attractive feature of the flux ratio is that typical values of γ can be estimated – and its properties rationalized – by means of linear stability analysis. For the z-independent elevator modes, the eddy-induced temperature and salinity fluxes are given by

$$\overline{w'T'} = \frac{1}{2}\hat{w}\hat{T},$$
$$\overline{w'S'} = \frac{1}{2}\hat{w}\hat{S}. \tag{2.11}$$
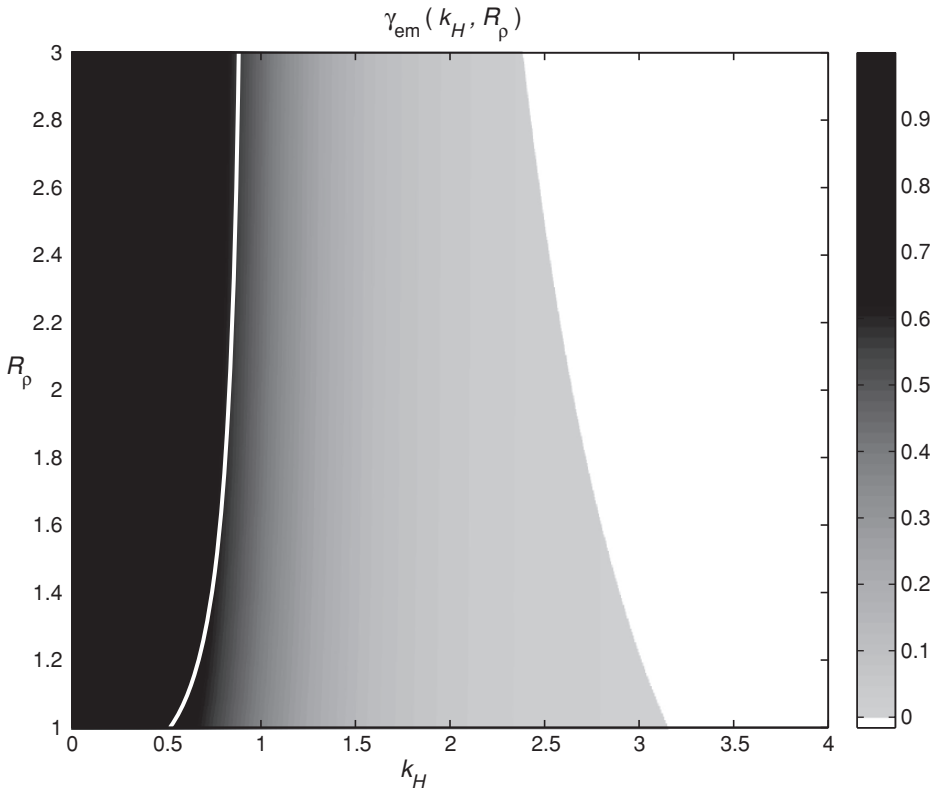
$$\gamma_{\text{em}}(k_H, R_\rho)$$

Figure 2.6 Flux ratio of the elevator mode as a function of the wavenumber and the density ratio. Only amplifying modes are shown. The white curve indicates the wavenumber of the fastest growing mode (k_{max}).

Therefore, the flux ratio of elevator modes reduces to $\gamma_{\text{em}} = \frac{\hat{T}}{\hat{S}}$. While the linear theory cannot determine the individual amplitudes of temperature ($\hat{T}$) and salinity ($\hat{S}$), each mode is characterized by a unique value of their ratio.

The pattern of flux ratio in the fingering regime is presented in Figure 2.6, where γ_{em} is plotted as a function of k_H and R_ρ for the amplifying ($\lambda > 0$) modes. Note that the flux ratio is always less than unity, which is consistent with the energetics of the system. In order to support the growth of unstable modes, the potential energy lost by the haline stratification should exceed the energy gained by the thermal stratification. Note the monotonic decrease of the flux ratio with increasing wavenumber (k_H). This dependence can be readily rationalized by focusing on the difference in thermal dissipation of thin (high k_H) and thick (low k_H) fingers (Schmitt, 1979a). Thin fingers rapidly lose their temperature anomaly due to lateral diffusion and therefore can support only limited eddy heat flux. As a result, the flux
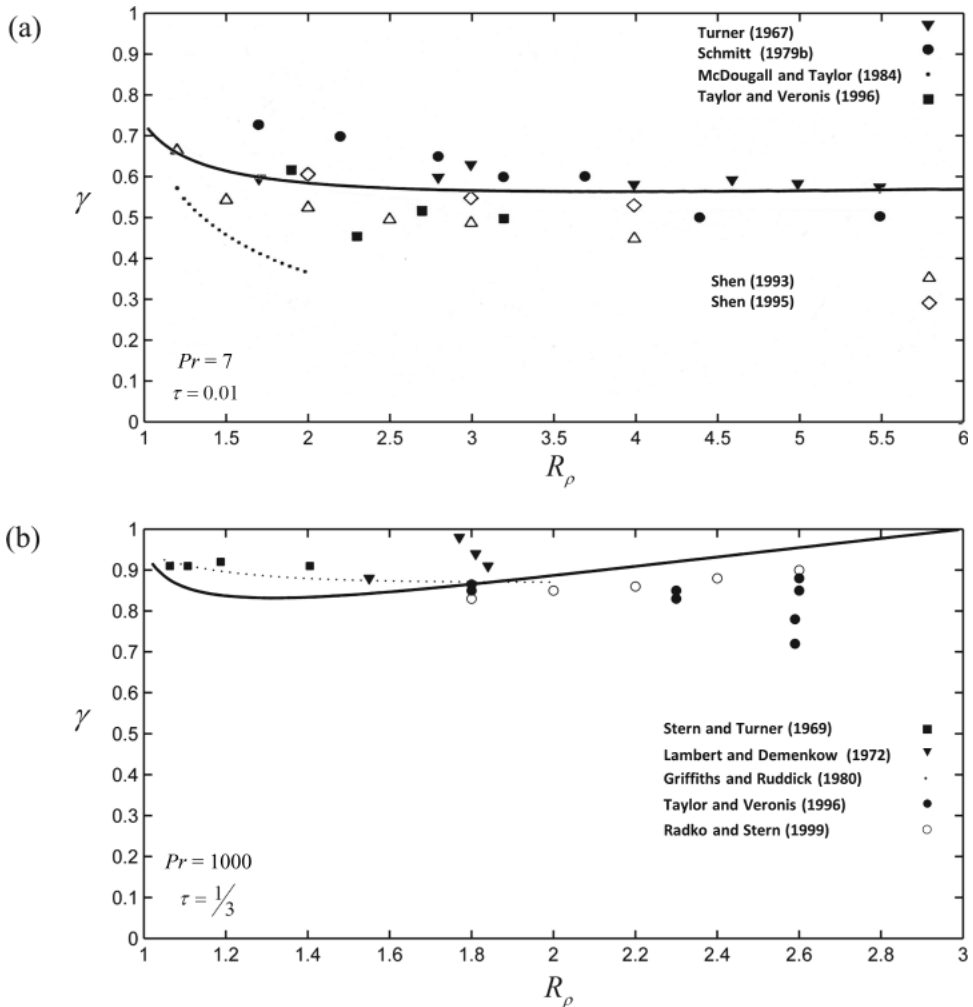
Figure 2.7 Salt-finger flux ratio as a function of the density ratio. Symbols are from laboratory and numerical experiments and the solid curves represent the theoretical estimates based on the fastest growing finger model. Calculations are made for (a) the oceanographic (heat–salt) parameters $(\tau, Pr) = (0.01, 7)$ and (b) salt–sugar parameters $(\tau, Pr) = (^1/_3, 10^3)$. After Kunze (2003).

ratio (2.7) is low. Wide fingers, on the other hand, can carry a larger temperature anomaly and will thus have a higher flux ratio. The preferred (fastest growing) fingers operate on intermediate scales and are characterized by a mid-range flux ratio.

Figure 2.7 shows the flux ratio of the fastest growing elevator modes ($k_H = k_{max}$) along with the flux ratios evaluated from a series of laboratory and numerical experiments. Presented are two cases. The oceanographic heat–salt system $(\tau, Pr) = (0.01, 7)$ is in Figure 2.7a. Both experimental and theoretical values of

the flux ratio in Figure 2.7a are in the $\gamma = 0.5-0.8$ range. The flux ratio decreases with R_ρ for $1 < R_\rho < 3$ and then remains nearly flat with a shallow minimum at $R_\rho \approx 4$. For larger density ratios (not shown) the flux ratio of the elevator mode gradually increases with R_ρ towards $\gamma_{\text{em}} = 1$ at $R_\rho \to \tau^{-1}$. The second calculation (Fig. 2.7b) was made for $(\tau, Pr) = (\frac{1}{3}, 10^3)$. This parameter set corresponds to the laboratory experiments in which heat and salt are replaced by aqueous solutions of sugar and salt as diffusing substances. Such experiments were introduced (Stern and Turner, 1969) to avoid problems associated with the heat loss across the walls of an experimental container, and sugar–salt systems still remain popular in laboratory studies (e.g., Krishnamurti, 2003, 2009). The salt–sugar flux ratio ($\gamma \sim 0.9$) is considerably higher than that for heat and salt. This tendency can be seen clearly in experiments and it is nicely reflected by the fastest growing mode theory. The pattern of the salt–sugar $\gamma(R_\rho)$ relation is also non-monotonic. As the density ratio increases from unity, the flux ratio first decreases, reaches minimum in the interior of the salt-finger interval, and then starts to increase towards unity. The location of the minimum, however, is shifted for the salt–sugar case to a much lower density ratio ($R_{\text{min}} \approx 1.3$) than for heat and salt. The quantitative differences in the flux ratio for heat–salt and sugar–salt systems underscore the sensitivity of salt fingering to the molecular characteristics of working fluids. The dependence of double-diffusive fluxes and structures on (τ, Pr) will be examined in greater detail in our review of non-oceanographic applications (Chapter 12).

Overall, for both heat–salt and salt–sugar systems, the predictions of the elevator mode theory are consistent with the corresponding laboratory and numerical experiments. This result is by no means trivial. Laboratory experiments are characterized by a broad spectrum of fully developed nonlinearly interacting modes that are not represented in the single-mode theory. The experimental validation of the theoretical model is highly valuable as it demonstrates the central role played by the fastest growing elevator modes in fingering dynamics.

2.4 Effects of horizontal gradients

A natural extension of the stability analysis is afforded by inclusion of horizontal background temperature and salinity gradients. For simplicity, we illustrate key effects using the two-dimensional (x, z) model, which does not lead to loss of generality – the three-dimensional linear stability problem can be reduced to its two-dimensional equivalent using a simple algebraic transformation (Holyer, 1983).

In order to construct a well-defined steady state, horizontal gradients are assumed to be density compensating:

$$\alpha \bar{T}_x = \beta \bar{S}_x. \tag{2.12}$$

For $\bar{T}_z > 0$, the non-dimensional governing equations for perturbation quantities take the form

$$\begin{cases} \dfrac{1}{Pr}\left(\dfrac{\partial \vec{v}}{\partial t} + \vec{v}\cdot\nabla\vec{v}\right) = -\nabla p + (T' - S')\vec{k} + \nabla^2\vec{v}, \\[2mm] \dfrac{\partial T'}{\partial t} + \vec{v}\cdot\nabla T' + Gu + w = \nabla^2 T', \\[2mm] \dfrac{\partial S'}{\partial t} + \vec{v}\cdot\nabla S' + Gu + \dfrac{w}{R_\rho} = \tau\nabla^2 S', \\[2mm] \nabla\cdot\vec{v} = 0, \end{cases} \qquad (2.13)$$

where $G = \frac{\bar{T}_x}{\bar{T}_z}$ represents the slope of isotherms in the basic state. The influence of horizontal gradients is reflected by the Gu terms in the temperature and salinity equations, terms that do not appear in the corresponding system for the horizontally uniform basic state (1.12).

As previously, system (2.13) is linearized and its stability is examined using the normal modes (2.1), which leads to the growth rate equation:

$$\lambda^3 + [1 + \tau + Pr]\kappa^2\lambda^2 + \left[(\tau + Pr + \tau Pr)\kappa^4 + Prk^2\kappa^{-2}\left(1 - R_\rho^{-1}\right)\right]\lambda$$
$$+ \tau Pr\kappa^6 - Prk^2\left(R_\rho^{-1} - \tau\right) + PrGkm(1 - \tau) = 0. \qquad (2.14)$$

Typical values of the slopes of isotherms in the ocean are quite low ($G \sim 10^{-3}$). Hence, if the vertical stratification supports fingering instability, the addition of lateral gradients has very limited effect on linear stability characteristics. The maximal growth rates and preferred wavelengths of fingers change by a fraction of a percent. However, fundamentally new effects come into play when vertical stratification is double-diffusively stable.

Figure 2.8a presents the growth rate pattern for $R_\rho = -1$ ($Tu = 0$). An extended region in the (k, m) space is occupied by the unstable ($\lambda > 0$) modes. Since vertical temperature and salinity gradients are both stabilizing, the growing modes in Figure 2.8a can only be attributed to the horizontal stratification. In contrast to the horizontally uniform case (Section 2.2), the fastest growing modes in Figure 2.8a are of finite vertical extent $H_{\text{dim}} \sim \frac{2\pi}{m_{\text{max}}}d \sim 2\text{m}$. They grow much slower than salt fingers (cf. Fig. 2.2) and operate on significantly larger spatial scales. The orientation of wave fronts in the fastest growing mode is nearly horizontal, with slopes of $s = -\frac{k_{\text{max}}}{m_{\text{max}}} \sim 2\cdot 10^{-4}$, and therefore these instabilities are best described as molecularly driven intrusions. Growing modes are found only for $s > 0$, which means that intrusions in the doubly stable ($\bar{T}_z > 0$, $\bar{S}_z < 0$) vertical gradient are oriented in the same sense as salinity contours and opposite to that of isotherms. Figure 2.8b presents an analogous example for a diffusively stratified ($\bar{T}_z < 0$, $\bar{S}_z < 0$) fluid. The diffusive density ratio in this case is $R_\rho^* = 3$ and therefore horizontally
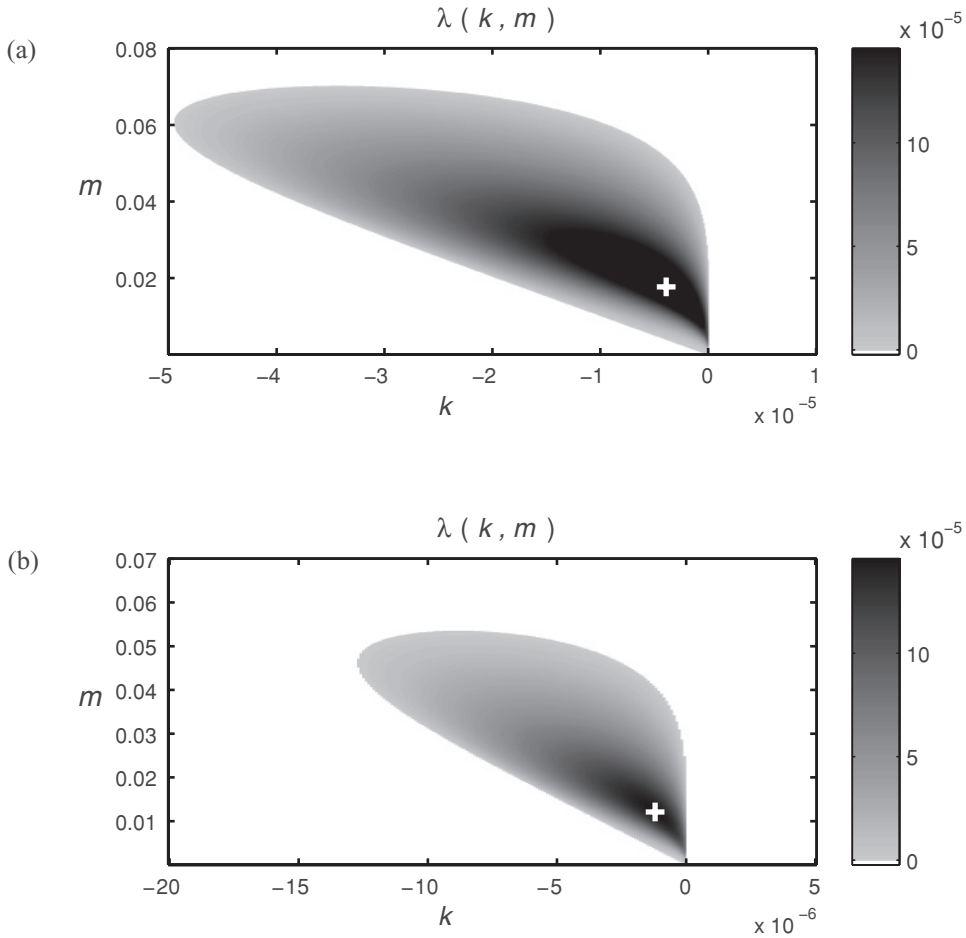
Figure 2.8 Destabilizing effects of horizontal gradients for the heat–salt system $(\tau, Pr) = (0.01, 7)$. Growth rate is plotted as a function of wavenumbers (k, m) for (a) doubly stable ($\bar{T}_z > 0$, $\bar{S}_z < 0$, $R_\rho = -1$) and (b) diffusive ($\bar{T}_z < 0$, $\bar{S}_z < 0$, $R_\rho^* = 3$) vertical stratification. In both cases, $G = \bar{T}_x / \bar{T}_z = 10^{-3}$. Only amplifying modes are shown and the maximal growth rates are indicated by the plus signs.

homogeneous stratification would be linearly stable according to (2.4). However, the inclusion of lateral gradients destabilizes the system. As in the doubly stable case (Fig. 2.8a), the instability comes in the form of interleaving currents. The wave fronts are slightly inclined relative to the horizontal in the same sense as the background isotherms.

The examples in Figure 2.8 illustrate a generic property of horizontally non-uniform double-diffusive systems. Lateral stratification, no matter how weak, always generates unstable interleaving modes. It should be noted in this regard that

horizontal *T–S* gradients are universally present in the ocean, although their magnitude is highly inhomogeneous. Thus, the entire ocean supports double-diffusion in one form or another. Growth rates of the molecularly driven intrusions are generally low (Fig. 2.8), particularly in comparison with the vertical (fingering or oscillatory) double-diffusive instabilities. Nevertheless, these instabilities serve an important role in ocean dynamics. For instance, it has been argued that molecularly driven interleaving is essential for the initiation of double-diffusive convection in regions where the vertical stratification is stable (Stern, 2003). Amplifying nearly horizontal modes perturb vertical stratification, eventually producing local vertical gradients that support much more intense vertical double-diffusive convection. This mechanism could be involved in the formation of Arctic and Antarctic thermohaline staircases – step-like patterns in vertical temperature and salinity profiles (Chapter 8). High-latitude diffusive staircases are observed in regions with generally moderate large-scale density ratios of $2 < R_\rho^* < 10$, which are linearly stable with respect to vertical double-diffusion. Stern (2003) proposed that weak lateral *T–S* gradients in such regions are essential for staircase formation – they generate molecularly driven intrusions that evolve into small-scale steps and subsequently merge into larger layers.

Another compelling reason to study molecularly driven intrusions is related to their dynamic similarity to intrusions driven by vertical eddy-induced *T–S* fluxes (Chapter 7). While eddy-induced intrusions are more intense and widespread in the ocean, their quantitative description is problematic in view of highly uncertain vertical flux laws. Such complications do not arise for molecularly driven intrusions since molecular dissipation is well represented by Fick's flux laws with known diffusivities. Therefore, a popular approach to the analysis of interleaving involves theoretical and laboratory investigation of molecularly driven intrusions (e.g., Thorpe *et al.*, 1969; Kerr, 1992). Such studies are often accompanied by imaginative, albeit fundamentally qualitative, extrapolations of the results to the problem of eddy-induced interleaving.

This discussion concludes our summary of linear models of double-diffusive convection. In this review we restrained from venturing into numerous generalizations of the classical theory. For instance, we have not considered extensions to multicomponent ($n > 2$) systems (Griffiths, 1979; Terrones and Pearlstein, 1989; Liang, 1995) and cross-diffusion effects, in which molecular diffusion of one diffusing substance is affected by the gradient of others (Hurle and Jakeman, 1971; McDougall, 1983; Liang *et al.*, 1994). Not considered here are temperature-dependent viscosity and diffusivity, which can affect the stability properties of both fingering and diffusive systems (Tanny *et al.*, 1995). While such generalizations are undoubtedly of theoretical interest, they do not fundamentally change our understanding of double-diffusion, particularly for the oceanic (heat–salt) case.

Therefore, readers are referred to the original papers for details of the modified linear stability analysis. The content of this chapter has been selected to provide the essential background for the analysis of observations and for the nonlinear theory that is considered next. Nonlinear effects in double-diffusive convection are illustrated using three elementary geometric configurations: (i) the unbounded gradient model, (ii) the two-layer system and (iii) the model of a vertically bounded double-diffusive layer. Each model gets a chapter.